RSC Applied Interfaces

ROYAL SOCIETY OF CHEMISTRY

PAPER

View Article Online
View Journal | View Issue

Cite this: *RSC Appl. Interfaces*, 2025, **2**, 1758

Sustainable carbon–metal oxide composites from waste sources: synthesis, characterization, and mechanical properties

Subhabrata Senapati,[a] Sharmistha Anwar,[b] Vijay Singh Parihar, *[c] Rama Kanta Layek, [d] P. K. Patra[e] and Mrityunjoy Mahato *[a]

Carbon–metal oxide composites are widely utilized as lightweight materials in aerospace, automotive, and sports equipment. Since the discovery of carbon nanotubes (CNTs) in 1991, exploration of CNTs and their incorporation into composites has gained attention; however, large-scale, cost-effective production and property control remain challenges. This study reports the thermocatalytic synthesis of Al_2O_3–CNT, Al_2O_3/Fe_2O_3–CNT, Fe_2O_3–C, and ZnO–C composites using waste plastic as a carbon source and aluminum cans and scrap iron for metal oxides. Characterization *via* UV-vis spectroscopy, SEM, TEM, EDX, Raman spectroscopy, XRD, and nanoindentation test confirms the material composition and structure. TEM and Raman spectroscopy reveal successful CNT formation in Al_2O_3 and Al_2O_3/Fe_2O_3 systems, while Fe_2O_3 and ZnO form CNT-free carbon composites. The Al_2O_3/Fe_2O_3–CNT composite shows a better density-normalized elastic modulus value, *i.e.* 9.66 GPa g^{-1} cm^3, in comparison to other samples. The elastic modulus values of Al_2O_3–CNT, Fe_2O_3–C, Al_2O_3/Fe_2O_3–CNT, and ZnO–C are found to be in the range 10.19 GPa to 23.31 GPa, whereas hardness is in the range 0.42 GPa to 0.75 GPa, and elastic recovery is in the range 8.1% to 28.9%. The higher I_G/I_D ratio of the Al_2O_3/Fe_2O_3–CNT composite (2.05) compared to other composites (1.5, 1.41, 1.4) reflects a higher quality and responsible parameter for the higher elastic modulus of Al_2O_3/Fe_2O_3–CNT. This work highlights a low-cost, waste-derived route to high-performance, lightweight carbon–metal oxide composites.

Received 24th February 2025,
Accepted 31st July 2025

DOI: 10.1039/d5lf00053j

rsc.li/RSCApplInter

1. Introduction

Metal oxide–carbon (MO–C) composites are emerging materials having application in the field of lightweight composites, batteries, supercapacitors, catalysis, environmental remediation, sensing, and water purification.[1–3] MO–C composites possess some excellent material properties such as high mechanical strength, large surface area, high conductivity, electrocatalytic activity *etc.*[4] MO–C composites are evolving as lightweight composite-based advanced materials due to their combination of structural durability, strength, reduced mass, enhanced toughness, and wear resistance.[5] The combination of carbon materials with metal oxides improves mechanical durability, high-temperature stability, and corrosion resistance, which are suitable for aerospace, automotive, construction, defense, sports equipment, and high-stress environments.[6–8] Carbon materials especially CNTs have received great attention after their discovery in 1991[9] due to their remarkable properties like high elastic modulus (~1 TPa), tensile strength (150 GPa),[10] high electrical conductivity (~10^6 S m^{-1}),[11] high surface area (~1315 m^2 g^{-1}),[12] low density (lightweight) (~1.3 g cm^{-3}), quantum confinement effect due to their small diameter (1.33–2 nm for SWCNT), and chemical inertness.

In the fast-paced world of engineering and manufacturing, the search for innovative materials with higher mechanical performance while reducing weight has become a top priority.[5] These types of materials are referred to as lightweight composites (LCs), which is defined by the density-normalized mechanical strength (E/ρ). The LCs have high mechanical strength with light weight and corrosion resistance.[13] The average elastic modulus (E) of steel is 210 GPa, density (ρ) is 7.83 g cm^{-3}, and the ratio of elastic

[a] *Physics Division, Department of Basic Sciences and Social Sciences, School of Technology, North-Eastern Hill University, Shillong, Meghalaya, 793022, India. E-mail: mrityunjoyphy@gmail.com*
[b] *Advanced Materials Technology Department, CSIR-Institute of Minerals and Materials Technology, Bhubaneswar 751013, India*
[c] *Biomaterials and Tissue Engineering Group, Faculty of Medicine and Health Technology, Tampere University, 33720, Tampere, Finland. E-mail: vijay.parihar@tuni.fi*
[d] *Department of Separation Science, School of Engineering Science, LUT University, Mukkulankatu 19, 15210, Lahti, Finland*
[e] *Department of Physics, School of Physical Sciences, North-Eastern Hill University, Shillong, Meghalaya, 793022, India*

modulus to density, *i.e.* density-normalized mechanical strength, of steel is 28 GPa cm^3 g^{-1}.[14] Steel has high mechanical strength; however, it is a heavyweight material, which limits its applications in many sectors including aerospace, sports equipment, defense materials, transport vehicles *etc.* Carbon-based materials such as CNTs were recognised as components of LCs due to their high elastic modulus (~1 TPa), which is approximately five times higher than that of steel, and low density of 1.3 g cm^{-3}, and one-sixth that of steel.[10]

The density and elastic modulus of a material are considered to be crucial in the automotive sector from the point of view of weight and strength. According to the US Department of Energy, 10% reduction in vehicle weight results in 6–8% reduction in fuel consumption and 8% reduction in CO_2 emission.[15] In this regard, LCs play a crucial role in enhancing fuel efficiency and reducing CO_2 emission in the automotive sector. Aluminum and magnesium alloys along with polymer–metallic fiber composites are preferred LCs in the automotive sector. Recently, Briggs Automotive and Ford Motors used graphene composites to make stronger components for their vehicles.[16] The LCs are classified as metal matrix composites (MMCs), polymer matrix composites (PMCs), ceramic matrix composites (CMCs), and fiber matrix composites (FMCs).[17] MMCs using CNTs and graphene are more effective than alloys due to high wear resistance, high operating temperature, lightweight composite useful in fighter aircraft, unmanned aerial vehicles (UAVs), ballistic missiles *etc.*[17,18] Fiberglass plastic, carbon fiber reinforced polymer composites, and aramid fiber composites are commonly used lightweight materials in aerospace industries.[19,20] There are reports on the use of CNTs and graphene in concrete to enhance their compressive strength, tensile strength, modulus of elasticity, flexural strength, porosity, electrical conductivity, autogenous shrinkage properties, *etc.*[21]

Understanding the mechanical properties of CNT-based composites is crucial for optimizing their performance.[22] The elastic modulus of nanocomposites depends on various factors such as shape, size, composition, defects, synthesis method *etc.* Also, the elastic modulus value depends on the techniques used, such as atomic force microscopy (AFM), three-point or four-point bend test, nanoindentation test, *etc.* It is to be noted that the elastic modulus of iron, steel and iron oxide is reported to be 205 GPa, 210 GPa, and 217 GPa, respectively.[23] The elastic modulus of aluminum and aluminum oxide is 253 GPa and 379 GPa, respectively.[24] Researchers have reported the mechanical properties of various carbon composites, *e.g.*, Awotunde *et al.* reported the elastic modulus of NiAl-CNT as 7.20 GPa.[25] Maron *et al.* studied different combinations of epoxy–ZnS–CNT composites with elastic modulus as 9.38–14.32 GPa.[26] Bakshi *et al.* found the elastic modulus of Al–Si–CNT composite as 4.95 to 5.95 GPa.[27] Carreño-Morelli *et al.* studied the elastic modulus of Mg-CNT composites and found the value of *E* as 38.60 GPa.[28]

The synthesis of quality and defect-free CNTs and their incorporation in the composites were explored since their discovery in 1991; however, large-scale, low-cost synthesis and property control are still challenging. Pyrolysis-based chemical vapor deposition (CVD) is still considered to be a relatively larger-scale technique to synthesize CNTs using a variety of carbon sources and catalysts.[29–31] The low-cost synthesis of CNTs demands for the use of low-cost catalysts such as iron and aluminum. For example, Alexiadis *et al.* reported the synthesis of CNT by the CVD of ethylene gas using the Al_2O_3/Fe_2O_3 catalyst,[29] where the carbon precursor is catalytically broken down on the surface of the catalyst to grow CNTs. Hosseini *et al.* also reported the synthesis of CNTs by catalytic decomposition of ethylene gas using the Al_2O_3/Fe_2O_3 catalyst.[32] The growth of CNT bundles is reported by Shukrullah *et al.* using the Al_2O_3/Fe_2O_3 catalyst for the decomposition of ethylene gas.[33] However, the CNT diameter was reported to be more than 200 nm, which is beyond the nano range (<100 nm). To the best of our knowledge, no report has focused on the use of low-cost waste-derived carbon source and waste-based or naturally abundant catalysts to synthesize CNT bundles with diameters within the nanoscale range (<100 nm).

In this paper, four different CNT/C based composites, namely Al_2O_3–CNT, Fe_2O_3–C, Al_2O_3/Fe_2O_3–CNT, and ZnO–C, were synthesized using a pyrolysis technique and low-cost carbon sources like waste plastics due to their high carbon content of 60–90 wt% depending on the type of plastic. Al_2O_3 and Fe_2O_3 were synthesized from waste-derived sources such as waste aluminum cans and scrap iron, respectively, due to the abundance of suitable precursors, simple and low-cost processing methods. In contrast, ZnO was synthesized from zinc salt and not from waste source because zinc-containing wastes are less abundant, often hazardous (*e.g.*, containing Cd or Pb), and require complex, multi-step extraction processes. Overall, the present work follows SDG goal number 9 (industry, innovation, and infrastructure), 12 (responsible consumption and production) and 13 (climate action). In our earlier report, the elastic modulus of some CNT composites was measured by a Raman-based non-destructive technique.[34] The metal oxide catalyst and MO–C composites were characterized by UV-vis spectroscopy, SEM, TEM, EDX, Raman spectroscopy, and XRD technique. The mechanical properties were characterized by nanoindentation technique. EDX confirmed the purity of the composites, TEM confirmed CNT formation in the presence of Al_2O_3 and Al_2O_3/Fe_2O_3 catalysts, whereas Fe_2O_3 and ZnO facilitated formation of amorphous carbon, *i.e.* Fe_2O_3–C and ZnO–C, composites, as confirmed by Raman spectroscopy and TEM. The elastic modulus of different carbon–metal oxide composites was found to be in the range of 10.19–23.31 GPa, density-normalized elastic modulus is in the range 4.22–9.66 GPa g^{-1} cm^3, hardness is in the range 0.42 GPa to 0.75 GPa, and elastic recovery is in the range 8.1% to 28.9%. The

higher I_G/I_D ratio of the Al_2O_3/Fe_2O_3–CNT composite (2.05) compared to other composites (1.5, 1.41, 1.4) reflects the higher quality and responsible parameter for the higher elastic modulus of Al_2O_3/Fe_2O_3–CNT.

2. Experimental

2.1. Materials

HDPE waste plastics were used as a source of carbon, which were cut into 1 cm × 1 cm pieces. Waste beverage Al cans were cut into 2 cm × 2 cm dimensions. All these materials were separately cleaned with running tap water, soap solution and DI water (pH 6.5, resistivity 18.2 MΩ) before drying in a hot air oven. The required chemicals such as hydrochloric acid (HCl, 37% AR grade), sulphuric acid (H_2SO_4, 50% extra pure), nitric acid (HNO_3, 69%), zinc nitrate ($Zn(NO_3)_2$), sodium hydroxide (NaOH, 98%), ammonium hydroxide (NH_4-OH, 25%), and ethanol (absolute, 99.9%) were purchased from Merck, India.

2.2. Synthesis of Al_2O_3 nanocatalyst

Aluminum oxide was prepared from waste Al cans; typically, 40 g Al can pieces (2 cm × 2 cm) were treated with 100 mL 50% H_2SO_4 to remove any surface contaminants like paint and internal polyacrylic coatings present.[35] Further, 40% NaOH solution was added to the acid-rinsed cans by vigorous stirring, and sodium meta aluminate dihydrate ($Na[Al(OH)_4]$) solution was formed during the process. 68% HCl was added dropwise into the solution and stirred properly to adjust the pH of 7 and a white gelatinous precipitate was formed, which was washed several times with DI water and ethanol. The gel was then dried in a hot air oven and calcined at 600 °C for 3 h. After calcination, the off-white colored Al_2O_3 powder was collected and kept for further use.

$$2Al + 2NaOH(aq.) + 6H_2O \rightarrow 2Na[Al(OH)_4] + 3H_2(\uparrow) \quad (1)$$

$$2Na[Al(OH)_4] + HCl \rightarrow Al(OH)_3 + H_2O + NaCl \quad (2)$$

$$Al(OH)_3 \xrightarrow[\text{At 600 °C}]{\text{Dried and calcined}} Al_2O_3 + 3H_2O(\uparrow) \quad (3)$$

2.3. Synthesis of Fe_2O_3 nanocatalyst

Iron oxide was synthesized using waste iron. Typically, 40 g waste iron (washed and dried) was added to 60 mL 35% HCl with manual stirring due to its magnetic nature and heated at 70 °C for liberation of Fe^{2+} and Fe^{3+} ions.[36] It was treated with 20 mL 68% HNO_3 to convert Fe^{2+} ions to Fe^{3+} ions. NH_4OH was further added to it to obtain a brown-colored precipitate of ferric hydroxide [$Fe(OH)_3$]. The obtained precipitate was washed several times with a DI water and ethanol mixture and dried in a hot air oven. The dried $Fe(OH)_3$ was taken for calcination at 600 °C for 3 h. The red-colored Fe_2O_3 powder was collected and kept for further use.

$$Fe + 2HCl \rightarrow FeCl_3 + H_2 \quad (4)$$

$$2Fe + 6HCl \xrightarrow{65\ ^\circ C} 2FeCl_3 + 3H_2 \quad (5)$$

$$Fe^{2+} \xrightarrow{HNO_3} Fe^{3+} \quad (6)$$

$$Fe^{3+} + 3NH_4OH \rightarrow Fe(OH)_3 + 3NH^{4+} \quad (7)$$

$$2Fe(OH)_3 \xrightarrow[\text{At 600 °C}]{\text{Dried and calcined}} Fe_2O_3 + 3H_2O \quad (8)$$

2.4. Synthesis of Al_2O_3/Fe_2O_3 nanocatalyst

Aluminum oxide–iron oxide (Al_2O_3–Fe_2O_3) composite was prepared using a mixture of 70 g waste Al (70 wt%) and 30 g waste iron (30 wt%) by a co-precipitation method. 150 mL of 35% HCl was added to the mixture with continuous manual stirring as iron is magnetic. The acid-mixed solution was further treated with 40 mL 68% HNO_3 to convert the Fe^{2+} to Fe^{3+} ions. This solution was again treated with NH_4OH to obtain a light-brown-colored precipitate, which was washed several times in a DI water–ethanol mixture and dried in a hot air oven. The dried precipitate was calcined for 4 h at 600 °C. The obtained material was recognized as Al_2O_3/Fe_2O_3 composite and kept for further application.

2.5. Synthesis of ZnO nanocatalyst

Microwave-assisted irradiation is a low-cost, time-saving technique for the synthesis of nanomaterials and was adopted here to prepare zinc oxide (ZnO) nanocatalyst.[37] Zinc nitrate ($Zn(NO_3)_2$) was dissolved in DI water to prepare a 0.1 M solution of zinc hydroxyl. Liquid NH_4OH was added dropwise to the above solution to maintain its pH at 8. The product was washed several times with a mixture of DI water and ethanol. The obtained precipitate was exposed to radiation for 5 minutes in a domestic microwave oven, yielding a white-colored product. Subsequently, the sample was dried for 6 hours at 120 °C in a hot air oven and kept for further application.

$$2Zn(NO_3)_2 \xrightarrow{\text{Microwave irradiated}} 2ZnO + 4NO_2 + O_2 \quad (9)$$

2.6. Synthesis of carbon–metal oxide composite

Waste HDPE plastic and different metal oxide nanocatalysts were used in a custom-made pyrolysis reactor to prepare MO–CNT/C composites following an earlier report with a little modification.[38,39] The HDPE and catalysts were taken in a 2 : 1 ratio, typically 1 g and 500 mg, respectively, in a silica boat under a N_2 atmosphere with a flow rate of 100 mL min^{-1}. The reactor was heated up to 800 °C with a heating rate of 10 °C min^{-1} and was kept constant at 800 °C for 1.5 h to complete the deposition process. The reactor was allowed to cool gradually with a cooling rate of 2–5 °C min^{-1} overnight and the black-colored nanocatalyst–MWCNT composites were collected and kept for further analysis. The approximate yield of CNT + catalyst was ~40% in the batch mode reactor.

2.7. Fabrication of carbon–MO composite pellet

Initially, PVA gel was prepared by mixing 500 mg PVA powder into 10 mL of DI water. The PVA gel was mixed with the composite powder and air-dried for a few minutes and then cold-pressed into 10 mm diameter cylindrical pellets using a hydraulic press at 50 kg m^{-2} pressure. The pellets were then calcined at 600 °C for 3 h. The pellets were further polished using sandpaper and velvet cloth and used for nanoindentation.

2.8. Material characterization

The UV-vis absorption spectra were studied using a double beam UV-visible spectrophotometer (Hitachi, U 3900) in the range 200–800 nm. Surface morphology analysis of the carbon composite powder samples was carried out by field emission scanning electron microscopy (FESEM) (Zeiss, Supra 55). High-resolution transmission electron microscopy (HR-TEM) and energy-dispersive X-ray spectroscopy (EDS) images were recorded using an HR-TEM system (JEOL, JEM-2100). Raman spectra of the nanocatalyst–carbon composites were recorded by a laser micro-Raman system (Horiba Jobin Yvon, LabRam HR) using a diode laser of wavelength 532 nm with a spectrum range of 50–4000 cm^{-1} and a maximum resolution of 0.5 cm^{-1}. The nanoindentation study was carried out using a nanoindenter system (Bruker Germany, Hysitron TI premier) equipped with a Berkovich-type diamond indenter tip to study the elastic modulus and hardness of the composites.[40] The crystalline structure and formation of the phase of the composites were analyzed from XRD patterns using an X-ray diffractometer (Rigaku, Ultima IV, 40 KV).

3. Results and discussion

3.1. UV-visible spectroscopic study of CNT-MO composites

Fig. S1A shows the UV-vis spectrum of Al_2O_3–CNT, which shows an absorption shoulder around 210 nm.[41] The absence of distinct peaks and broad absorbance band corresponds to a non-specific absorbance across the UV-visible region, which may be due to the mixture of compounds, namely Al_2O_3–CNT. Fig. S1B shows the UV-vis spectra of the Fe_2O_3–C composite with two distinct absorption peaks at 219 nm and 243 nm, which may be due to the optical absorption of iron.[42] Fig. S1C shows the UV-vis spectra of the Al_2O_3/Fe_2O_3–CNT composite with a sharp absorbance peak at 237 nm, indicating a strong π–π* transition peak due to CNT formation.[43] Fig. S1D shows the UV-vis spectra of the ZnO–C composite with prominent peaks at 219 nm due to the presence of the π–π* transition of carbon[44] and at 375 nm due to the n–π* transition of the ZnO–C composite, which is observed at a shifted position compared to pure ZnO (35 nm).[43] Fig. S2 shows the band gap calculation through a Tauc plot, which is 4.05 eV, 4.66 eV, 3.94 eV and 2.33 eV for Al_2O_3–CNT, Fe_2O_3–C, Al_2O_3/Fe_2O_3–CNT, and ZnO–C, respectively. The band gap of pure Al_2O_3 is reported to be in the range 5.1–8.8 eV, depending on the phase and synthesis method,[45] which is reduced to 4.05 in combination with the composite Al_2O_3–CNT. The band gap of pure Fe_2O_3 is reported to be 2.1 eV,[46] which increased to 4.66 eV in composite with amorphous carbon. The band gap of Al_2O_3/Fe_2O_3–CNT is found to be 3.94 eV, which is in between the value of Al_2O_3 and CNT (1.19 eV)[47] due to band gap engineering. The band gap of ZnO is reported in the literature to be 3.3 eV,[48] which is further reduced to 2.5 eV in the ZnO–C composite. Overall, Tauc plot analysis indicated that the MO–C carbon composite impacted the band gap and electronic structures of the MOs.

3.2. FESEM and HRTEM study

The surface morphology and structure of the composite materials were studied using FESEM and HRTEM, respectively (Fig. 1). Fig. 1A shows the SEM image of Al_2O_3–CNT, which displays a morphology with large agglomerates of aluminum oxide particles, along with some tube- or needle-like structures of CNT with an average CNT diameter of 5 nm, which is confirmed in the HRTEM images (Fig. 1B). The TEM image of Al_2O_3–CNT shows clusters of Al_2O_3 particles along with the CNTs, as evidenced from EDS data. Fig. 1C shows the SEM image of the Fe_2O_3–C composite structure showing nanoscale particles packed together. There is no CNT-like structure seen in the composite from the TEM image and hence carbon observed from EDS data is basically amorphous carbon. Fig. 1D shows the TEM image indicating Fe_2O_3–C composite particles with an average size of 77 nm as confirmed in the EDS plot. It is seen as agglomerated nanoparticles since individual particles clump together to form larger aggregates.[49] Fig. 1E represents the SEM image of the Al_2O_3/Fe_2O_3–CNT composite which shows a tube-like network intertwined with one another and forming CNT bundles, which are identified using HRTEM (Fig. S3).

This kind of structure is desirable for high electrical conductivity, high surface area, or mechanical strength.[50] The narrow size distribution suggests a highly controlled synthesis process, producing nanoparticles embedded in a CNT network, which are beneficial for applications in catalysis or sensing, where high surface area and uniform particle size are advantageous.[2] Fig. 1F represents the TEM image of Al_2O_3/Fe_2O_3–CNT with an average CNT diameter of 20 nm, which forms bundles of CNTs with a thickness of 52 nm. The bundle-like nanostructure might serve as potentially useful for producing hybrid nanocomposites with enhanced surface areas. Fig. 1G shows the ZnO–C composite comprising particles and spike structures, which are found to be small ZnO nanorod structures or carbon needles under HRTEM (Fig. 1H). The dark needle-like structures suggest the presence of a metal nanoparticle which is ZnO in the composite and there is no presence of CNTs in the sample.

Fig. 2A shows EDS data from HRTEM of Al_2O_3–CNT, showing EDS peaks of Al, O, and C which confirms the presence of the oxide form of aluminum (Al_2O_3) in the sample. Fig. 2B shows EDS data of Fe_2O_3–C with the presence

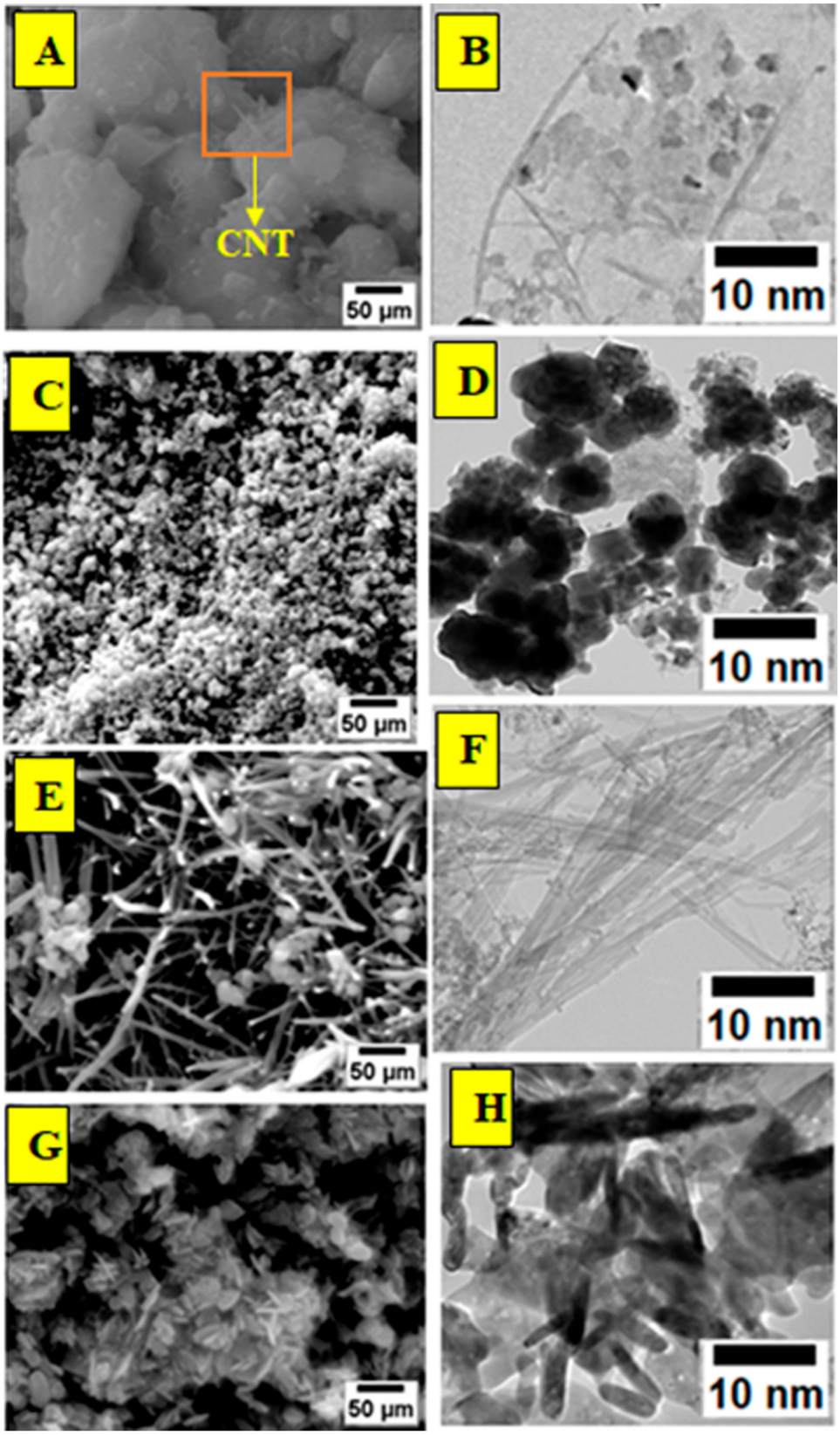

Fig. 1 (A and B) SEM and HRTEM images of Al_2O_3–CNT, (C and D) SEM and HRTEM images of Fe_2O_3–C, (E and F) SEM and HRTEM images of Al_2O_3/Fe_2O_3–CNT, and (G and H) SEM and HRTEM images of ZnO–C.

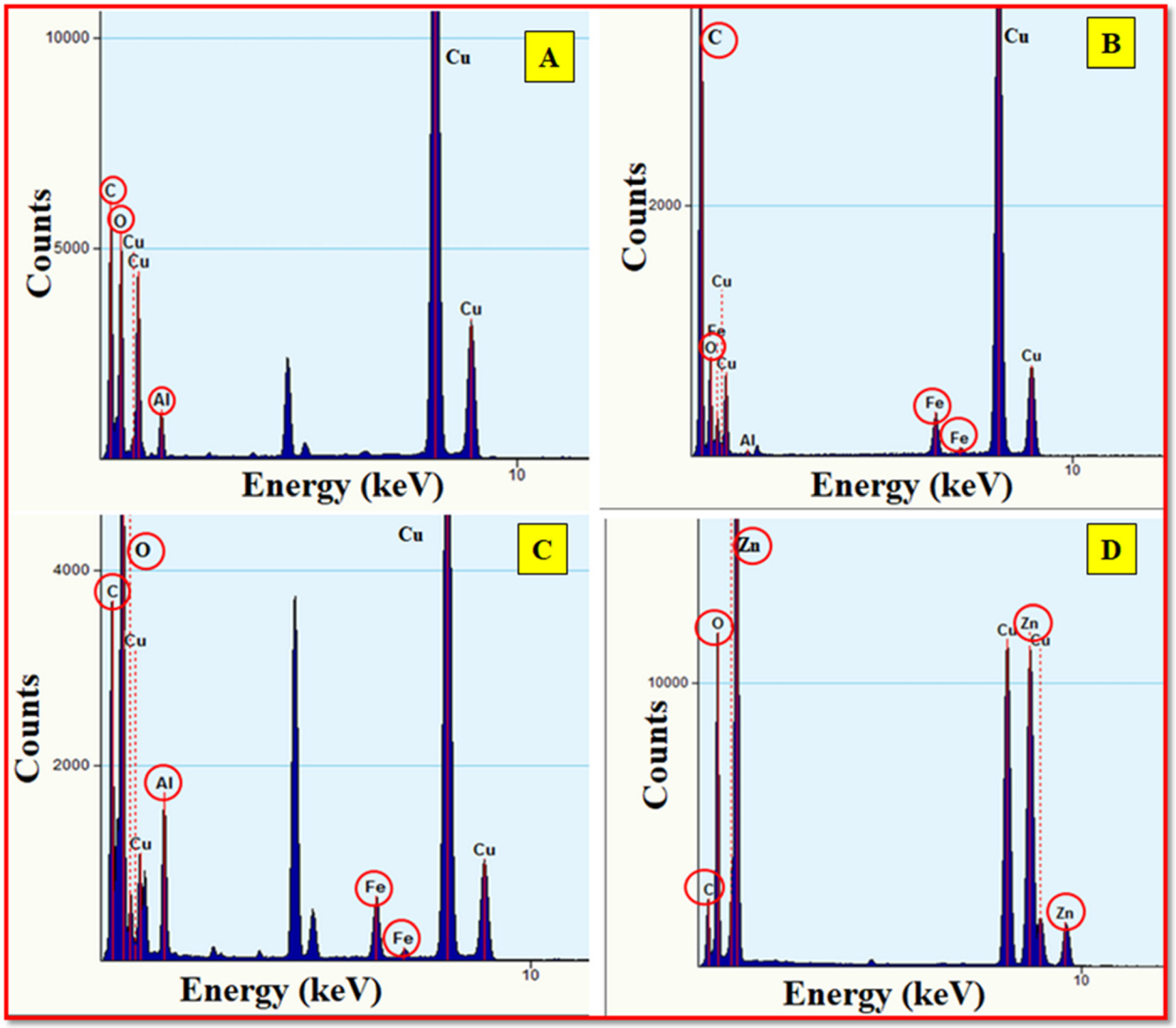

Fig. 2 Elemental analysis by energy-dispersive spectroscopy (EDS) of (A) Al_2O_3–CNT, (B) Fe_2O_3–C, (C) Al_2O_3/Fe_2O_3–CNT, and (D) ZnO–C.

of Fe, O, and C elements indicating iron oxide and carbon in the composite. Fig. 2C shows the EDS of Al_2O_3/Fe_2O_3–CNT with peaks of Al, Fe, O, and C in the EDS data, which confirms the presence of aluminum oxide and iron oxide along with CNTs in the composite material in line with an earlier report.[51] Fig. 2D shows the presence of C, Zn, and O in the EDS, which indicates the formation of zinc oxide in the ZnO–C sample. The presence of Cu in every EDS image is due to the use of a Cu grid during TEM characterisation. The presence of the required elements and absence of unwanted elements in each EDS image shows the purity of the samples, although the composites were extracted from waste materials. The presence of carbon in every sample confirms the presence of either CNTs or carbon in the composites, which is further confirmed from TEM images. The presence of O indicates the formation of oxide in every sample. The presence of Cu is due to the Cu grid used during TEM characterisation.

Fig. S4 shows the TEM images of different composites, which indicates a fairly uniform distribution of Al_2O_3, Fe_2O_3, ZnO, CNTs, and carbon in all composites in the nanoscale. Al_2O_3–CNT and ZnO–C composites display good dispersion with CNTs and carbon phases, respectively. The Al_2O_3–Fe_2O_3–CNT composite shows a mixed phase distribution with minor Fe_2O_3 clustering. Overall, oxide phases dominate (~70%) along with CNT or carbon phases (~30%) with good dispersion and networking. The distribution of constituent phases in the composites is also supported by the SEM images (Fig. 1) at micron scale areas with good dispersion and network. Fig. S5 shows the *d*-spacing analysis from the TEM fringe pattern for the confirmation of different metal oxides, which are found to be 0.304 nm/0.50 nm (d-Al_2O_3),[52,53] 0.30 nm/0.38 nm (Fe_2O_3),[54] and 0.250 nm (ZnO),[55] in line with the cited earlier reports. The *d*-spacing calculation of different oxides from the TEM fringe pattern confirms their authentic presence in their respective composite. The thickness of the ZnO–C composite was measured with the help of AFM in order to further clarify the needle-like structure to be made of carbon or ZnO structure,

although AFM has limitations in distinguishing the same. The measurement was taken at three different places, as shown in Fig. S6, and the composite was found in the form of nanoflakes with an average thickness 40 nm, which may be ZnO needle composite with carbon.

3.3. X-ray diffraction study

The crystallographic structures of the carbon–MO composites were investigated using powder X-ray diffraction (XRD) technique (Fig. 3). The sharp diffraction peaks indicate the high crystalline nature of the materials. The peaks around 27.30–27.45° (Fig. S7) are assigned to the (002) plane due to the presence of graphitic structure (JCPDS file 75-2078). In the XRD pattern of Al_2O_3–CNT, the (002) plane of CNT coincides with the (012) plane of Al_2O_3; hence it is difficult to identify the peaks separately.[56] In Al_2O_3–CNT, the carbide phase of the material, *i.e.* Al_4C_3, is also found at 32.2° and 56.9°, which correspond to the (200) and (116) planes, respectively.[57] A summary of the XRD peak positions, lattice planes, and phases of Al_2O_3–CNT, Fe_2O_3–C, Al_2O_3/Fe_2O_3–CNT, and ZnO–CNT are provided in Table S1. From the XRD spectra of Al_2O_3–CNT and Fe_2O_3–C, it is concluded that Al_2O_3 (JCPDS file 71-1123) is in the alpha phase,[56] whereas Fe_2O_3 (JCPDS file 19-0629) is in the gamma phase.[58] The XRD pattern of Al_2O_3/Fe_2O_3–CNT shows the presence of both iron and aluminum phases as mentioned in Table S1. The XRD pattern of the ZnO–C composite represents ZnO as a hexagonal wurtzite structure (JCPDS file 36-1451).[59]

3.4. Raman spectroscopic study

Raman spectroscopy is a nondestructive experimental technique to characterize the carbon and carbon-based composite materials due to sensitivity to detect the disordered carbon materials using the vibrational frequencies of atomic bonds.[60] The Raman spectra of the different carbon composites Al_2O_3–CNT, Fe_2O_3–C, Al_2O_3/Fe_2O_3–CNT, and ZnO–C are shown in Fig. 4 along with their characteristic D and G bands in the range of 1000–1800 cm^{-1}. The two characteristic bands of the Raman spectra emerged from disorder or diamond-like carbon (D band) and graphite-like carbon (G band), respectively.[61] The positions of the D and G bands and the ratio of their intensities are given in Table 1. The D band is a double resonance Raman mode that arises due to out-of-plane vibrations and is used to quantify the degree of structural disorder of the carbon material.[2,62] The intensity of the D band depends upon the energy of the laser used in the Raman spectrometer and the phonon density of states, which further leads to the symmetry breaking phenomena of the unit cell of the sp^2 carbon nanomaterials.[63,64] In MWCNTs, the D band is associated with the structural defects of the tube and the G band is considered to be a tangential Raman mode that arises due to in-plane stretching vibration of the C–C bond within the sp^2 carbon nanomaterials. The G band has some kind of dependency on the types of carbon material.[65] The different Raman bands are summarised in Table S2. The peaks in the region 250–750 cm^{-1} of the Raman spectra are due to the asymmetric stretching of metal and oxide groups present in the sample.[66] The Raman peaks at 435–445 cm^{-1} are attributed to second-order Raman (E_{2H}) mode and at 612–670 cm^{-1} are attributed to the surface optical (SO) phonon modes.[67] The presence of Raman vibrations due to metal oxide along with the G and D bands confirms the formation of carbon composite.[66] The intensity of the G and D bands in Raman spectroscopy is crucial for understanding the structural characteristics of carbon-based materials like CNT, graphene, graphite, *etc.* The G band-to-D band ratio (I_G/I_D) is a well-defined parameter and was calculated to quantify the structural defects, purity and graphitization of carbon nanomaterials from deconvoluted Raman spectra (Fig. S8). The I_G/I_D ratio indicates the degree of carbon graphitization in the composites and a higher value of the ratio indicates better graphitization or superior quality of the carbon composites.[68] It is to be noted that the deconvoluted Raman spectra can also be used to calculate elastic modulus using Raman deconvoluted parameters and density parameters, as reported in an earlier report.[34] The higher I_G/I_D ratio of the Al_2O_3/Fe_2O_3–CNT composite (2.05) compared to other composites (1.5, 1.41, 1.47) is indicative of the higher quality of CNTs, leading to a higher elastic modulus as discussed in a later section (Fig. 5 and S8).

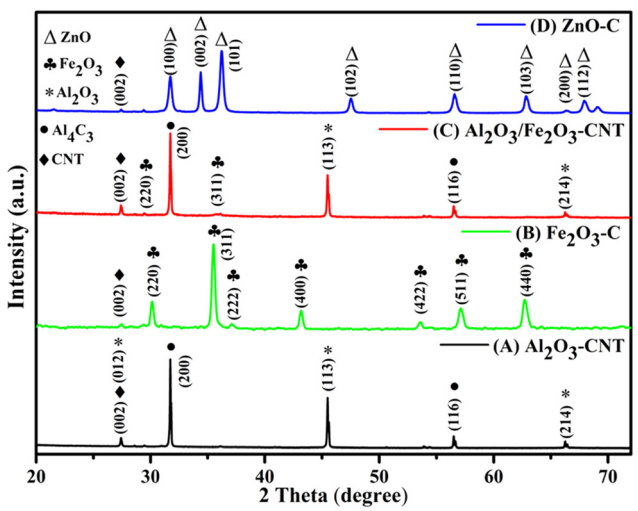

Fig. 3 XRD patterns of different carbon composites: (A) Al_2O_3–CNT, (B) Fe_2O_3–C, (C) Al_2O_3/Fe_2O_3–CNT, and (D) ZnO–C.

3.5. Nanoindentation study for elastic modulus (E) and hardness (H) of carbon–MO composites

Nanoindentation is widely used for MO-carbon composites and there are several reports on CNT composites such as NiAl–CNT,[30] Al–CNT,[69,70] and CNT-polymer composites.[71] Nanoindentation offers significant advantages over other mechanical testing methods: capable of nanoscale measurement, minimal test area, allows for depth profiling,

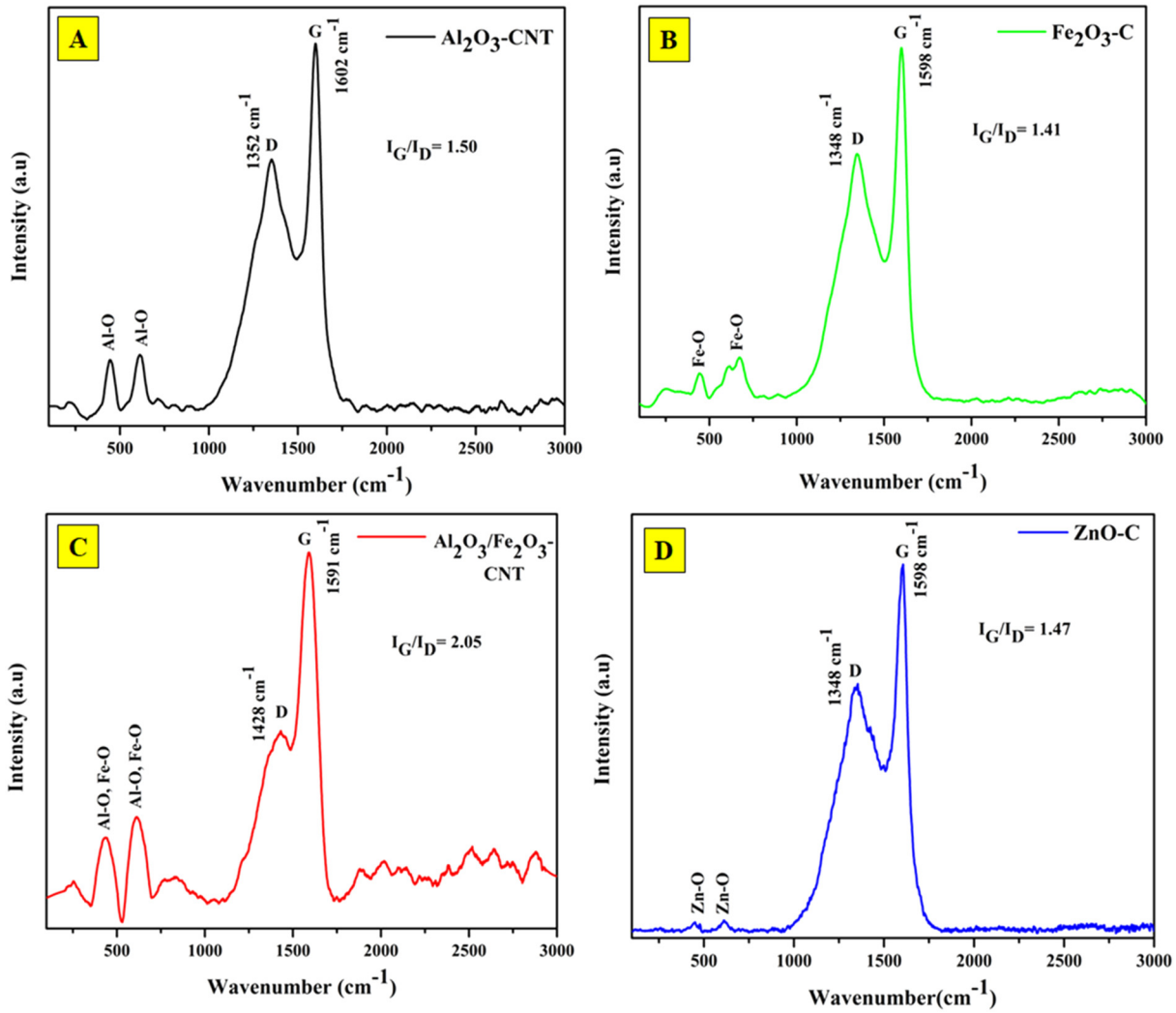

Fig. 4 Raman spectra of (A) Al_2O_3–CNT, (B) Fe_2O_3–C, (C) Al_2O_3/Fe_2O_3–CNT, and (D) ZnO–C composites.

can target individual microstructural features like grains or phases, allows precise measurement of mechanical properties at the nanoscale and hence suitable for thin films, coatings, and nanocomposites.[69–71] The hardness (H) and elastic modulus (E) of the nanocomposites were determined from the nanoindentation load–displacement curve using the Oliver and Pharr method.[72] Fig. S9 shows a schematic load–displacement curve, which indicates the response of material to applied stress, both elastically and plastically. The area enclosed by the loading and unloading curve in region 1 represents the energy

Table 1 Summary of mechanical parameters of different carbon–MO composites from the present work and the literature

CNT composites	E (GPa)	H (GPa)	H/E, H^3/E^2 (MPa)	W_e (%)	h_{max}, h_{res}	Method of testing	Reference
Al_2O_3–CNT	14.52	0.71	0.49, 1.60	20.31	334.30, 266.40	Nanoindentation	Present work
Fe_2O_3–C	10.19	0.42	0.40, 0.60	8.10	554.11, 509.21		
Al_2O_3/Fe_2O_3–CNT	23.31	0.75	0.31, 0.71	28.29	254.14, 182.22		
ZnO–C	11.67	0.45	0.38, 0.62	23.46	332.10, 224.32		
Al–5% CNT	35.78	3.08	—	—	—	Nanoindentation	74
Al–CNT	62.1 ± 20.4	0.51 ± 0.10	—	—	—	Nanoindentation	75
NiAl–CNT	7.20	0.13	—	—	—	Nanoindentation	30
NiAl–CNT	5.05	0.42	—	—	—		
Al–Si–5% CNT	4.95 ± 0.05	—	—	—	—	Compression test	32
Al–Si–10% CNT	5.65 ± 0.95	—	—	—	—		
Mg–CNT	38.60	—	—	—	—	Resonant bar test	33
Epoxy–ZnS–CNT	9.38–14.32	—	—	—	—	Tensile and impact test	31

absorbed by the composite due to plastic deformation. Initially, the deformation is primarily elastic (reversible), but as load increases beyond a certain point, plastic (permanent) deformation also occurs.[73] After reaching the maximum load, the indenter is gradually withdrawn from the material. The unloading curve shown in region II represents the elastic recovery of the material corresponding to the energy required for elastic recovery during deformation.[40] The slope of the unloading curve, especially near the start of unloading, can be used to calculate the reduced modulus of the material. The hardness of the nanocomposite can be calculated using the following eqn (10),[40] where H is the hardness of the material, P_{max} is the maximum load, and A is the contact area at that particular load during indentation.

$$H = \frac{P_{max}}{A} \tag{10}$$

The effective elastic modulus can be measured using the elastic deformation region shown in Fig. S6, using eqn (11),[40]

$$E_{eff} = \frac{\sqrt{\pi}S}{2\beta\sqrt{A}} \tag{11}$$

Here, β = 1.034 for the Berkovich tip, and S is the slope of the unloading curve in Fig. S6. The effective modulus is the combination of the elastic modulus of the sample and the indenter as per eqn (12),[40]

$$\frac{1}{E_{eff}} = \frac{1-\nu^2}{E} + \frac{1-\nu_i^2}{E_i} \tag{12}$$

where E_{eff} is the reduced elastic modulus, E is the elastic modulus of the sample, and E_i is the elastic modulus of the indenter, *i.e.* Berkovich tip, ν is the Poisson's ratio of the sample and ν_i is the Poisson's ratio of the indenter. The elastic modulus (E) and hardness (H) values can be used to calculate resistance to cracking (H/E), resistance to plastic deformation (H^3/E^2), and elastic recovery (W_e)[40] (eqn (13)), where h_{max} is the displacement at maximum load and h_{min} is the residual displacement after unloading.

$$W_e = \left(\frac{h_{max} - h_{min}}{h_{min}}\right) \times 100 \tag{13}$$

The elastic modulus (E) and hardness (H) of the materials were calculated from the slope of the unloading portion of the load–displacement curves of different carbon–MO nanocomposites using eqn (1) and (2) as shown in Fig. 5A and B and Table 1. Fig. 5B and Table 1 show the maximum values of E and H of Al_2O_3/Fe_2O_3–CNT (23.31 GPa, 0.75 GPa), and the Fe_2O_3–C composite achieved the lowest values (10.09 GPa, 0.42 GPa) among the four C–MO composites. The elastic modulus and hardness values of the composites are well correlated with their TEM observations.[40] The higher value of E and H of Al_2O_3/Fe_2O_3–CNT compared to other composites is due to the formation of higher- quality CNT bundles, as evident in the I_G/I_D ratio as well as from the TEM images. Other elastic parameters, such as resistance to cracking (H/E), resistance to plastic deformation (H^3/E^2), and elastic recovery (W_e) are also summarised in Table 1. These parameters are also important because they reflect the balance between hardness and elasticity of the materials. The elastic recovery percentage of Al_2O_3/Fe_2O_3–CNT is the highest (28.29%) and that of Fe_2O_3–CNT is the lowest (8.10%). It is evident from Table 1 that the material with the highest E value has the highest elastic recovery percentage. The average density of MO–CNT composites was calculated from literature density data of similar composites (Table S3). The density-normalized elastic modulus of the present MO–CNT composites was calculated and was compared with those of

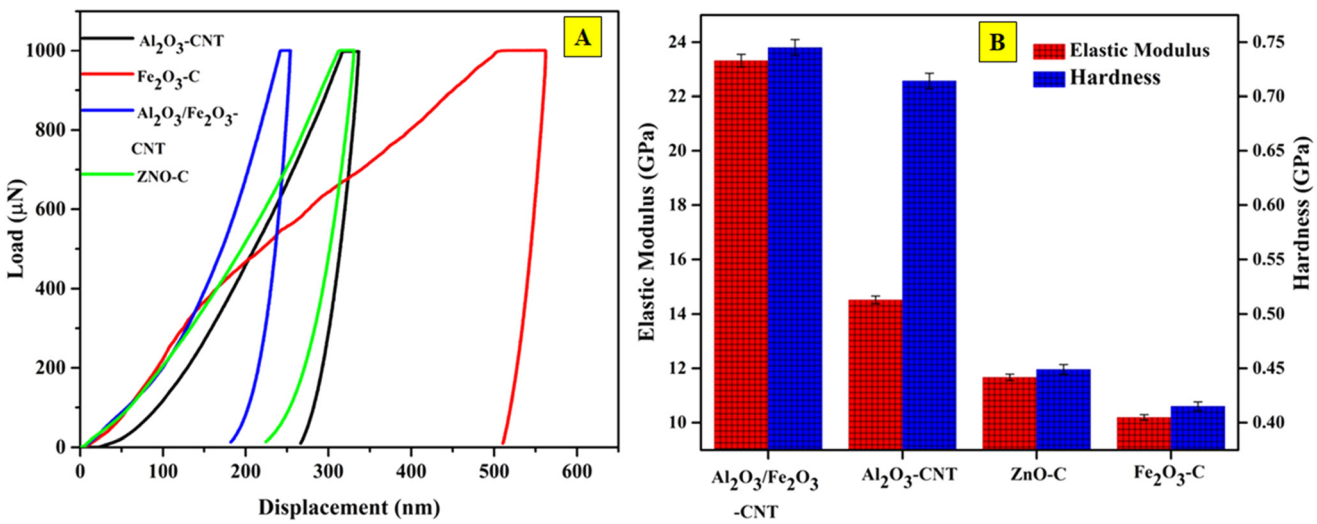

Fig. 5 (A) Load–displacement mechanical strength curves using the nanoindentation method. (B) Bar plot of elastic modulus and hardness of Al_2O_3–CNT, Fe_2O_3–C, Al_2O_3/Fe_2O_3–CNT, and ZnO–C.

traditional mechanical materials like steel, iron, and aluminum (Table S4).

The Fe_2O_3–C composite showed the highest fracture toughness and the lowest brittleness, as evidenced by its broad load–displacement curve and large deformation before failure. In contrast, Al_2O_3/Fe_2O_3–CNT exhibited the highest hardness and stiffness (bulk modulus) due to its steep curve and high peak load at low displacement, but also displayed the most brittle behavior with minimal energy absorption. Al_2O_3–CNT offered a balanced profile with moderate toughness and high hardness, while ZnO–C showed a moderate mechanical performance, suitable for applications requiring flexibility and strength. The elastic modulus of metal oxide-based composites, particularly those reinforced with carbon nanotubes (CNTs), can vary significantly depending on several factors including the type of metal oxide matrix, CNT dispersion, CNT quality, interfacial bonding, volume fraction of the reinforcement, and the overall microstructure. These variations highlight the role of composite structure in tailoring mechanical properties for specific applications.

3.6. Other potential applications of carbon–MO composites

The potential applications of carbon-metal oxide (C–MO) composites were explored and summarized with the help of literature reports.[76–79] In this regard, the synthesized composites, such as Al_2O_3–CNT, Al_2O_3/Fe_2O_3–CNT, Fe_2O_3–C, and ZnO–C, have potential applications in various emerging areas such as lightweight composites, batteries, supercapacitors, catalysis, environmental remediation, sensing, and water purification due to their excellent material properties such as high mechanical strength, large surface area, high conductivity, electrocatalytic activity, enhanced toughness, wear resistance, high-temperature stability, and corrosion resistance.[80–85] The electrocatalytic properties of carbon–metal oxide composites arise due to the high electrical conductivity and large surface area of carbon materials with the redox activity and catalytic sites of metal oxides. This leads to high charge transfer, increased number of active sites, and stability, facilitating different applications in energy storage and conversion areas such as fuel cells,[80] supercapacitors,[81] batteries,[82] gas sensing,[83] water splitting/hydrogen production,[84] photocatalysis[85] and light weight composites.[19,20,86,87]

4. Conclusions

Over the past few decades, the requirement of lightweight smart materials for different applications has been in the limelight. Aluminum, due to its lightweight nature and high mechanical strength, has become a suitable material in composites. In this work, four different carbon composites, namely Al_2O_3–CNT, Fe_2O_3–C, Al_2O_3/Fe_2O_3–CNT, and ZnO–C, were synthesized by a CVD-based technique and characterized by different complementary techniques. UV-vis absorption and XRD analyses of the composites suggest the presence of both carbon and metal oxide. FESEM, HRTEM and EDS show the presence of CNTs in Al_2O_3 and bundles of CNTs in Al_2O_3/Fe_2O_3 with an average diameter of 20 nm and 52 nm, respectively, whereas Fe_2O_3–C and ZnO–C are with amorphous carbon forms. Raman study suggests the superior quality of CNTs in the Al_2O_3/Fe_2O_3 catalyst. Nanoindentation technique is used to find the elastic modulus of the samples and, further, their density-normalized elastic modulus was calculated. The Al_2O_3/Fe_2O_3–C composite shows a better density-normalized elastic modulus value, *i.e.* 9.66 GPa g^{-1} cm^3, in comparison to other samples. The elastic modulus of Al_2O_3–CNT, Fe_2O_3–C, Al_2O_3/Fe_2O_3–CNT, and ZnO–C, is in the range 10.19 GPa to 23.31 GPa, whereas hardness is in the range 0.42 GPa to 0.75 GPa, and elastic recovery is in the range 8.1% to 28.9%. The higher I_G/I_D ratio of the Al_2O_3/Fe_2O_3–CNT composite (2.05) compared to other composites (1.5, 1.41, 1.4) reflects the higher quality and responsible parameter for the higher elastic modulus of Al_2O_3/Fe_2O_3–CNT. The present work contributes to advancing the area of sustainable and lightweight composite materials.

Author contributions

Subhabrata Senapati: material preparation, characterization, analysis, draft writing. Sharmistha Anwar: mechanical characterization and analysis. Vijay Singh Parihar: editing, manuscript preparation. Rama Kanta Layek: data analysis. P. K. Patra: conceptualization, editing. Mrityunjoy Mahato: final manuscript, project handling, analysis, editing.

Conflicts of interest

There are no conflicts of interest to declare.

Data availability

Supplementary information: SI comprises of nine figures containing UV-visible spectrocopy, band gap from Tauc plot, TEM cropped images for CNT bundle, TEM images for distribution of constituent phases, TEM images for *d*-value calculation, zoom XRD for 26 degree carbon peak, AFM images for ZnO–C composite only, deconvoluted Raman D, G band, schematic loading–unloading curve for plastic, elastic region. There are four tables in the SI comprising XRD peak assignment, Raman peak assignment, average density calculation, and density normalized elastic modulas. See DOI: **https://doi.org/10.1039/D5LF00053J**.

The datasets generated and/or analyzed during this study will be available in the Trepo, the institutional repository of Tampere University (**https://trepo.tuni.fi/**). Additionally, the data are available upon reasonable request.

Acknowledgements

MM would like to acknowledge SERB, Govt of India (File No: SIR/2022/001615) and ANRF, Govt of India (ANRF/PAIR/2025/000010/PAIR-B). VSP would like to acknowledge the Research

Council of Finland for funding support through the Centre of Excellence in Body-on-Chip Research (CoEBoC) at Tampere University (decisions #312409). We would also like to acknowledge Siksha O Anusandhan (SOA) University for SEM and XRD, AIIMS, New Delhi, for TEM, and CIF IIT, Guwahati, for Raman spectroscopy.

References

1 S. Jovanović, M. Huskić, D. Kepić, M. Yasir and K. Haddadi, *Graphene and 2D Materials*, 2023, **8**(3), 59–80.
2 A. Shah, Y. M. Mao, L. R. Singh, M. Gogoi and M. Mahato, *Carbon Lett.*, 2022, **32**, 1541–1557.
3 A. Nath, A. Shah, L. R. Singh and M. Mahato, *Nanotechnol. Environ. Eng.*, 2021, **6**, 70.
4 E. Zapata-Solvas, D. Gómez-García and A. Domínguez-Rodríguez, *J. Eur. Ceram. Soc.*, 2012, **32**(12), 3001–3020.
5 X. Gong, Z. Cao, M. Zeng, X. Zou, Y. Yang and H. Yan, *J. Mater. Sci.*, 2022, **57**(35), 16675–16689.
6 W. Zhang and J. Xu, *Mater. Des.*, 2022, **221**, 110994.
7 V. R. A. Prakash, M. Bourchak, H. Alshahrani and K. A. Juhany, *Biomass Convers. Biorefin.*, 2023, **14**, 31895–31906.
8 A. V. Radhamani, H. C. Lau and S. Ramakrishna, *Composites, Part A*, 2018, **114**, 170–187.
9 S. Iijima, *Nature*, 1991, **354**, 56–58.
10 Y. Jung, Y. S. Cho, J. H. Park, J. Y. Cheon, J. W. Lee, J. H. Kim, C. R. Park, T. Kim and S. J. Yang, *Nano Lett.*, 2023, **23**(8), 3128–3136.
11 Y. Wang and G. J. Weng, *Micromechanics and Nanomechanics of Composite Solids*, ed. S. A. Meguid and G. J. Weng, Springer International Publishing, 2018, pp. 1–34.
12 A. Shah, S. Senapati, H. A. Murthy, L. R. Singh and M. Mahato, *ACS Omega*, 2023, **8**(37), 33380–33391.
13 I. A. Alnaser, *Sci. Rep.*, 2024, **14**(1), 19875.
14 H. T. Wang, N. R. Tao and K. Lu, *Scr. Mater.*, 2013, **68**(1), 22–27.
15 W. J. Joost, *JOM*, 2012, **64**, 1032–1038.
16 W. Zhang and J. Xu, *Mater. Des.*, 2022, **221**, 110994.
17 S. Siengchin, *Def. Technol.*, 2023, **24**, 1–17.
18 A. Sazrhi, R. O. Bura and G. Amperiawan, IEEE 6th Asian Conference on Defence Technology (ACDT), 2019, pp. 162–168.
19 M. Joshi and U. Chatterjee, Polymer nanocomposite: an advanced material for aerospace applications, in *Advanced composite materials for aerospace engineering*, Woodhead Publishing, 2016, pp. 241–264.
20 N. Kumar and A. Dixit, Nanomaterials-Enabled Lightweight Military Platforms, in *Nanotechnology for defence applications*, Springer International Publishing, 2019, DOI: **10.1007/978-3-030-29880-7_6**.
21 R. Siddique and A. Mehta, *Constr. Build. Mater.*, 2014, **50**, 116–129.
22 A. Kausar, I. Rafique and B. Muhammad, *Polym.-Plast. Technol. Eng.*, 2016, **55**(11), 1167–1191.
23 A. Ouglova, Y. Berthaud, M. François and F. Foct, *Corros. Sci.*, 2006, **48**(12), 3988–4000.
24 P. Gudlur, A. Forness, J. Lentz, M. Radovic and A. Muliana, *Mater. Sci. Eng., A*, 2012, **531**, 18–27.
25 M. A. Awotunde, A. O. Adegbenjo, O. O. Ayodele, A. M. Okoro, M. B. Shongwe and M. A. Olubambi, *J. Alloys Compd.*, 2019, **803**, 514–526.
26 G. K. Maron, B. S. Noremberg, J. H. Alano, F. R. Pereira, V. G. Deon, R. C. R. Santos, V. N. Freire, A. Valentini and N. L. V. Carreno, *Polym. Bull.*, 2018, **75**, 1619–1633.
27 S. R. Bakshi, A. K. Keshri and A. Agarwal, *Mater. Sci. Eng., A*, 2011, **528**(9), 3375–3384.
28 E. Carreño-Morelli, J. Yang, E. Couteau, K. Hernadi, J. W. Seo, C. Bonjour, L. Forro and R. Schaller, *Phys. Status Solidi A*, 2004, **20**(8), R53–R55.
29 V. I. Alexiadis and X. E. Verykios, *Mater. Chem. Phys.*, 2009, **117**, 528–532.
30 H. J. Das, A. Shah, L. R. Singh and M. Mahato, *Mater. Today: Proc.*, 2021, **47**, 1072–1077.
31 A. Nath and M. Mahato, *Mater. Today: Proc.*, 2022, **57**, 321–327.
32 A. A. Hosseini, F. S. Abhari and F. Taleshi, *Sci. J. Phys.*, 2011, **2012**, 1–8.
33 S. Shukrullah, N. M. Mohamed and M. S. Shaharun, *Appl. Mech. Mater.*, 2015, **695**, 122–126.
34 S. Senapati, A. Shah, P. K. Patra and M. Mahato, *Fullerenes, Nanotubes Carbon Nanostruct.*, 2022, **30**(2), 290–296.
35 R. López-Juárez, N. Razo-Perez, T. Pérez-Juache, O. Hernandez-Cristobal and S. Y. Reyes-López, *Results Phys.*, 2018, **11**, 1075–1079.
36 D. Mhamane, H. K. Kim, V. Aravindan, K. C. Roh, M. Srinivasan and K. B. Kim, *Green Chem.*, 2016, **18**(5), 1395–1404.
37 T. Prakash, R. Jayaprakash, G. Neri and S. Kumar, *J. Nanopart.*, 2013, **2013**, 1–8.
38 M. Mahato, M. Gogoi, A. Shah and S. Mandal, *India Pat.*, TEMP/E-1/20464/2021-KOL, 2021.
39 K. V. Sankar and R. K. Selvan, *RSC Adv.*, 2014, **4**, 17555–17566.
40 S. Anwar, S. Anwar, B. Nayak and R. S. Sankar, *Mater. Sci. Eng., B*, 2022, **284**, 115893.
41 A. Dunga, R. Koona and S. V. Naidu, *J. Nanofluids*, 2022, **11**(1), 58–73.
42 J. Samuel, A. Shah, D. Kumar, L. R. Singh and M. Mahato, *Mater. Today: Proc.*, 2021, **47**, 1048–1053.
43 O. E. Fayemi, A. S. Adekunle and E. E. Ebenso, *J. Biosens. Bioelectron.*, 2015, **6**(4), 1000190.
44 Z. Tan, H. Chihara, C. Koike, H. Abe, K. Kaneko, K. Sato and S. Ohara, *Astron. J.*, 2010, **140**(5), 1456.
45 E. O. Filatova and A. S. Konashuk, *J. Phys. Chem. C*, 2015, **119**(35), 20755–20761.
46 C. Xia, Y. Jia, M. Tao and Q. Zhang, *Phys. Lett. A*, 2013, **377**(31–33), 1943–1947.
47 Q. Lin, C. Gilardi, S. K. Su, Z. Zhang, E. Chen, P. Bandaru, A. Kummel, I. Radu, S. Mitra, G. Pitner and H.-S. P. Wong, *ACS Nano*, 2023, **17**(21), 21083–21092.

48 Y. Wu, D. B. Zhang, Z. Zhao, J. Pei and B. P. Zhang, *J. Eur. Ceram. Soc.*, 2021, **41**(2), 1324–1331.
49 S. Shrestha, B. Wang and P. Dutta, *Adv. Colloid Interface Sci.*, 2020, **279**, 102162.
50 A. M. K. Esawi, K. Morsi, A. Sayed, M. Taher and S. Lanka, *Composites, Part A*, 2011, **42**, 234–243.
51 R. Khanna, M. Ikram-Ul-Haq, S. Seetharaman and V. Sahajwalla, *ISIJ Int.*, 2016, **56**(7), 1300–1302.
52 Y. Rozita, R. Brydson, T. P. Comyn, A. J. Scott, C. Hammond, A. Brown, S. Chauruka, A. Hassanpour, N. P. Young, A. I. Kirkland and H. Sawada, *ChemCatChem*, 2013, **5**(9), 2695–2706.
53 M. Sun, A. E. Nelson and J. Adjaye, *J. Phys. Chem. B*, 2006, **110**(5), 2310–2317.
54 A. Nath, M. Mahato, L. R. Singh, P. K. Kuiri and M. Mahato, *Inorg. Nano-Met. Chem.*, 2025, **55**(2), 178–191.
55 F. Zoladz, S. Rhodes, D. Patterson, W. Cribb, P. Chapagain, D. Seifu, V. Taufour, S. Kamali and S. Neupane, *J. Nanopart. Res.*, 2020, **22**, 1–9.
56 Y. Shan, B. Pu, E. Liu, C. Shi, C. He and N. Zhao, *Mater. Sci. Eng., A*, 2020, **797**, 140058.
57 N. Yan, X. Zhou, Y. Li, F. Wang, H. Zhong, H. Wang and Q. Chen, *Sci. Rep.*, 2013, **3**(1), 3392.
58 S. M. Abbas, S. T. Hussain, S. Ali, N. Ahmad, N. Ali and S. Abbas, *J. Mater. Sci.*, 2013, **48**, 5429–5436.
59 F. V. Ferreira, W. Francisco, B. R. Menezes, F. S. Brito, A. S. Coutinho, L. S. Cividanes, A. R. Coutinho and G. P. Thim, *Appl. Surf. Sci.*, 2016, **389**, 921–929.
60 S. A. Chernyak, A. S. Ivanov, K. I. Maslakov, A. V. Egorov, Z. Shen, S. S. Savilov and V. V. Lunin, *Phys. Chem. Chem. Phys.*, 2017, **19**, 2276–2285.
61 P. Gill and N. Munroe, *J. Mater. Eng. Perform.*, 2012, **21**, 2467–2471.
62 S. D. M. Brown, A. Jorio, M. S. Dresselhaus and G. Dresselhaus, *Phys. Rev. B: Condens. Matter Mater. Phys.*, 2001, **64**, 073403.
63 Q. Zhao and H. D. Wagner, *Philos. Trans. R. Soc., A*, 2004, **362**(1824), 2407–2424.
64 M. Szybowicz, A. B. Nowicka and A. Dychalska, *Characterization of Nanomaterials*, Woodhead Publishing, 2018, pp. 1–36.
65 D. K. Padhi and K. Parida, *J. Mater. Chem. A*, 2014, **2**(26), 10300–10312.
66 P. Pandey, M. R. Parra, F. Z. Haque and R. Kurchania, *J. Mater. Sci.: Mater. Electron.*, 2017, **28**, 1537–1545.
67 D. C. D. Nath and V. Sahajwalla, *Mater. Sci. Appl.*, 2012, **3**, 103–109.
68 M. Sharma and V. Sharma, *Int. J. Miner., Metall. Mater.*, 2016, **23**, 222–233.
69 Y. Chen, S. R. Bakshi and A. Agarwal, *Surf. Coat. Technol.*, 2010, **204**(16–17), 2709–2715.
70 A. E. Moumen, M. Tarfaoui and K. Lafdi, *Composites, Part B*, 2017, **114**, 1–7.
71 W. C. Oliver and G. M. Pharr, *J. Mater. Res.*, 1992, **7**, 1564–1583.
72 T. K. Gupta, B. P. Singh, S. R. Dhakate, V. N. Singh and R. B. Mathur, *J. Mater. Chem. A*, 2013, **1**, 9138–9149.
73 J. Huang, N. Zhu, T. Yang, T. Zhang, P. Wu and Z. Dang, *Biosens. Bioelectron.*, 2015, **72**, 332–339.
74 M. Zhi, C. Xiang, J. Li, M. Li and N. Wu, *Nanoscale*, 2013, **5**(1), 72–88.
75 H. Zhou, L. Zhang, D. Zhang, S. Chen, P. R. Coxon, X. He, M. Coto, H. K. Kim, K. Xi and S. Ding, *Sci. Rep.*, 2016, **6**(1), 37752.
76 N. M. Hung, N. D. Chinh, T. Dai Nguyen, E. T. Kim, G. Choi, C. Kim and D. Kim, *Ceram. Int.*, 2020, **46**(18), 29233–29243.
77 N. I. Andersen, A. Serov and P. Atanassov, *Appl. Catal., B*, 2015, **163**, 623–627.
78 M. Lan, G. Fan, W. Sun and F. Li, *Appl. Surf. Sci.*, 2013, **282**, 937–946.
79 S. Y. Reyes-López, R. S. Acuña, R. López-Juárez and J. S. Rodríguez, *J. Ceram. Process. Res.*, 2013, **14**(5), 627–631.
80 A. S. Zayed, B. M. Kamel, T. Abdelsadek Osman, O. A. Elkady and S. Ali, *Fullerenes, Nanotubes Carbon Nanostruct.*, 2019, **27**(7), 538–544.
81 C. He, N. Zhao, C. Shi, X. Du, J. Li, H. Li and Q. Cui, *Adv. Mater.*, 2007, **19**(8), 1128–1132.
82 S. Münstermann, Y. Feng and W. Bleck, *Can. Metall. Q.*, 2014, **53**(3), 264–273.
83 R. H. Amra, A. H. Awad, A. M. Elsabbagh and M. Taha, *Int. J. Mater. Tech. Innov.*, 2024, **4**(2), 60–68.
84 A. K. Hasan, T. A. Jumah and K. M. Wadi, *Jordan J. Phys.*, 2025, **18**(1), 61–71.
85 G. R. Chate, R. M. Kulkarni, M. P. G. Chandrashekarappa, A. Lakshmikanthan, H. M. Harsha, S. Tophakhane, N. Shaikh, S. Kongi and P. Iranavar, *Fractur. Struct. Integr.*, 2022, **16**(60), 229–242.
86 S. Takaki, T. Masumura and T. Tsuchiyama, *J. Iron Steel Inst. Jpn.*, 2020, **106**(9), 89–92.
87 A. Ouglova, Y. Berthaud, M. François and F. Foct, *Corros. Sci.*, 2006, **48**(12), 3988–4000.